

Lifetime measurements of high-spin states in ^{101}Ag and their interpretation in the interacting boson fermion plus broken pair model

E. Galindo, M. Hausmann, A. Jungclaus,* D. Kast, K. P. Lieb, G. A. Müller, and O. Yordanov†
II. Physikalisches Institut, Universität Göttingen, Bunsenstrasse 7-9, D-37073 Göttingen, Germany

S. Brant and D. Vretenar
Department of Physics, Faculty of Sciences, University of Zagreb, 10000 Zagreb, Croatia

A. Algora, F. Brandolini, G. de Angelis, M. De Poli, C. Fahlander,‡ A. Gadea, T. Martinez, and D. R. Napoli
Istituto Nazionale di Fisica Nucleare, Laboratori Nazionali di Legnaro, I-35020 Legnaro, Italy

A. Dewald, R. Peusquens, and H. Tiesler
Institut für Kernphysik, Universität zu Köln, D-50937 Köln, Germany

M. Górska and H. Grawe
Gesellschaft für Schwerionenphysik, D-64291 Darmstadt, Germany

P. G. Bizzeti and P. Sona
Dipartimento di Fisica, Università di Firenze, and I.N.F.N., Sezione di Firenze, I-50125 Firenze, Italy

G. Bonsignori
Dipartimento di Fisica, Università di Bologna, and I.N.F.N., Sezione di Bologna, I-40126 Bologna, Italy

(Received 4 May 2001; published 2 August 2001)

Lifetimes of some 20 high-spin states in ^{101}Ag in the range between 0.2 and 200 ps have been measured using various Doppler shift techniques. The states have been populated in the reaction $^{58}\text{Ni}(^{50}\text{Cr}, \alpha 3p)$ at 200–205 MeV beam energy and their decays observed by means of the GASP array. For many states, the problem of their unknown side-feeding times has been circumvented by using the DDCM and NGTB $\gamma\gamma$ -coincidence methods. A total of some 60 reduced transition strengths or limits of them has been deduced. Moderately enhanced electric quadrupole transitions (up to 30 W.u.) have been derived as well as rather strong stretched magnetic dipole transitions within the negative parity yrast sequence (0.2–0.7) W.u. An attempt has been made to interpret the level energies and electromagnetic transitions within the interacting boson fermion plus broken pair model.

DOI: 10.1103/PhysRevC.64.034304

PACS number(s): 21.10.Tg, 21.10.Ky, 21.60.Fw, 27.60.+j

I. INTRODUCTION

The structures of high spin states in neutron-deficient nuclei below the Sn isotope chain, close to doubly-magic ^{100}Sn , are dominated by the interplay between proton holes in the $g_{9/2}$ orbit and neutrons distributed over several single-particle orbits extending in angular momentum from $j=1/2$ up to $j=11/2$. In nuclei close to $N=50$, this interplay can either be *competitive*, leading to well-separated families of either neutron particle or proton-hole configurations, or *co-operative* at higher spin values, where both spin-aligned protons and neutrons contribute to the total angular momenta of the states. Examples for this interplay have been established in the light In and Cd isotopes [1–6] for $N>50$ as well as in some $N=50$ isotones with $Z<50$ [7–10]. Given this situa-

tion, measurements of electromagnetic transition strengths and moments are most appropriate to check such multi-particle configurations, as we have recently demonstrated for a number of nuclides in this mass region, e.g., ^{94}Ru , ^{95}Rh , $^{102,104}\text{Cd}$, and $^{104,105}\text{In}$ [1–10]. Strongly retarded $E2$ and $M1$ transitions connecting families of different structures as well as $\Delta I=1$ cascades of strong magnetic dipole transitions have been established. The competition between proton holes and neutron particles and, in particular, the influence and number of active $h_{11/2}$ neutrons, relative to neutrons in lower- j orbits, turned out to sensitively depend on the so far unknown single-particle energies near ^{100}Sn . For increasing neutron number, collective vibrational motion and/or intruder states start to compete with shell model excitations.

The detailed lifetime measurements in ^{101}Ag ($Z=47$, $N=54$) using various Doppler shift attenuation and recoil techniques are based on the level scheme previously established by Crowell and collaborators [11]. As the result of this work, 18 lifetimes and four lifetime limits have been obtained, providing us with some 60 transition probabilities or limits of them. The level energies and transition strengths thus form a very valuable and broad basis for detailed model

*Present address: Consejo Superior de Investigaciones Científicas (CSIC) and Universidad Autónoma de Madrid, Madrid, Spain.

†Present address: GSI, D-64291 Darmstadt, Germany.

‡Also at Division of Cosmic and Subatomic Physics, Lund University, Lund, Sweden.

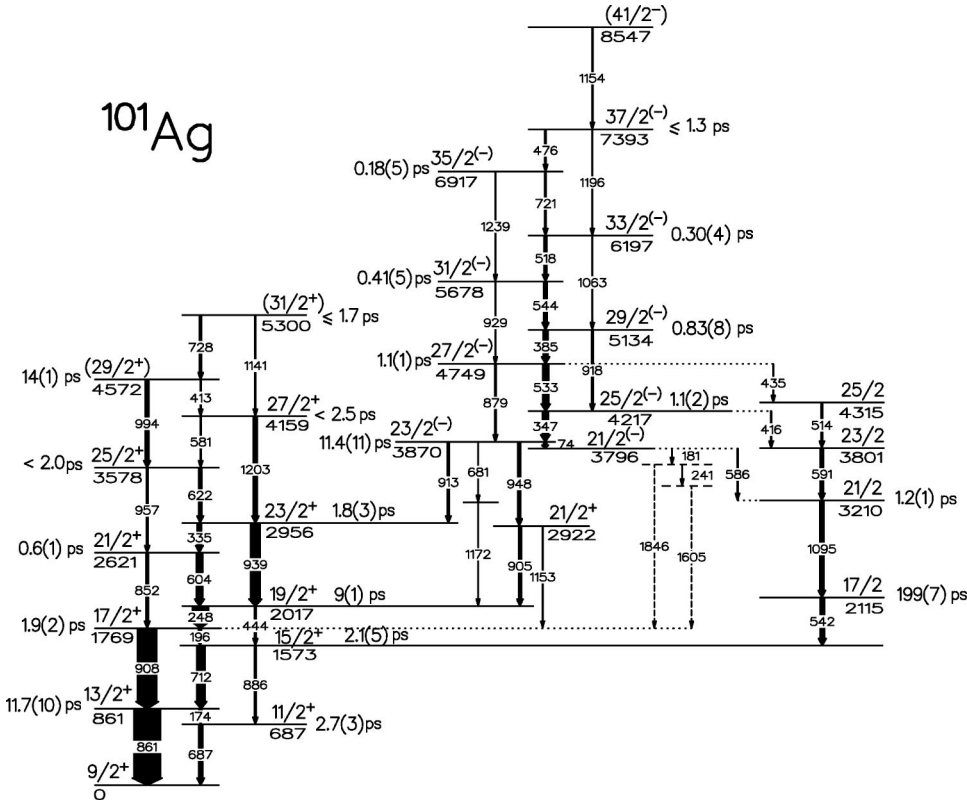


FIG. 1. Level scheme of ^{101}Ag used in the analysis as adopted from [11]. The lifetimes given are from the present work.

interpretations of this nucleus. In the present work, we have adopted the interacting boson fermion plus broken pair model (IBFBPM), which considers the interplay of collective and multiparticle components in the wave functions.

II. EXPERIMENTS

In the present lifetime study we employed the reaction $^{58}\text{Ni}(^{50}\text{Cr}, \alpha 3p)^{101}\text{Ag}$ at 205 MeV beam energy in a recoil distance doppler shift (RDDS) experiment and at 200 MeV in a Doppler Shift Attenuation (DSA) experiment [12]. The ~ 5 pA ^{50}Cr beam was provided by the XTU tandem accelerator of the Istituto Nazionale di Fisica Nucleare in Legnaro. In the RDDS experiment, we used a 1.2 mg/cm² thin self-supporting and stretched nickel target foil, enriched to 99.8% in the isotope ^{58}Ni , and a 12.3 mg/cm² stretched Au stopper foil, both foils being mounted in the University of Cologne plunger device [13]. A total of 12 plunger distances in the range between 16 μm and 7 mm were selected. The gamma radiation was detected in the GASP array [14], which contains 40 Compton-suppressed Ge detectors grouped into seven rings at the angles $\theta = 35^\circ, 59^\circ, 72^\circ, 90^\circ, 108^\circ, 121^\circ,$ and 145° relative to the beam direction. Through the analysis of unshifted and Doppler-shifted components of intense γ -ray transitions, the ^{101}Ag recoil velocity was deduced as $v/c = 3.11(5)\%$ of the speed of light. Further details of this experiment can be found in [5,6]. In the DSA experiment, a target consisting of a 1.0 mg/cm² thick ^{58}Ni layer (enrichment again 99.8%) on a 15 mg/cm² thick gold stopper foil was used. At both beam energies, the $^{101}\text{Ag} + \alpha 3p$ channel corresponds to the fifth strongest evaporation residue, after $^{104,102}\text{Cd}$ and $^{105,104}\text{In}$ [5,6]. As a result of this rather strong

population of states in ^{101}Ag , $\gamma\gamma$ -coincidence gating on various feeding and/or lower transitions was feasible in many cases, giving the possibility to use the so-called differential decay curve method (DDCM) in the coincidence mode [15,16] and/or the narrow gate on transition below (NGTB) Doppler shift technique [17], which avoid side-feeding problems, i.e., unknown side-feeding times (see below). At each recoil distance and for the Au-backed target, the $\gamma\gamma$ events were sorted into seven two fold $\gamma\gamma$ matrices with all 40 detectors of the array on one axis and the Ge detectors belonging to a particular ring of GASP on the other.

III. RESULTS

The level scheme of ^{101}Ag , as reported by Crowell and collaborators [11] and displayed in Fig. 1, was confirmed in the present work and used to establish the γ -ray flux through the high-spin cascades. The low-spin part of the level scheme, established by Kalshofen *et al.* [18] in the reaction $^{102}\text{Pd}(p, 2n)$, was not accessible to the present experiment. Two prominent level structures can be identified at high spin: the first one, with positive parity, is made up by cascades going from the $9/2^+$ ground state up to $(31/2^+)$, connected by regular, stretched $\Delta I = 1$ transitions $\Delta I = 2$ crossover. In this structure, the stretched $E2$ transitions are generally more intense than the $\Delta I = 1$ transitions. The high-spin sequence of presumed negative parity starts at $21/2^-$ and extends up to $(41/2^-)$. In this cascade, the $\Delta I = 1$ transitions clearly predominate in intensity over the $E2$ crossover transitions. For this second part of the level scheme, the negative parity was inferred by Crowell *et al.* [11], based on the similarity

with the negative band in ^{103}Ag [19].

Using the various Doppler shift techniques discussed below, a total of 18 lifetimes and four lifetime limits in the nucleus ^{101}Ag were measured in the time range of 0.2–200 ps, for states up to spin $37/2^{(-)}$. Prior to this work no lifetimes of excited states had been published. All the lifetime values are summarized in Table I. The reduced electromagnetic strengths obtained from the published branching ratios [11] are summarized in Table II.

A. The DDCM Analysis

The differential decay curve method [15,16] permits a direct analysis of lifetimes measured in a recoil distance Doppler shift experiment. In particular, DDCM is independent of side-feeding times, which in level structures dominated by shell model effects cannot be estimated or extrapolated in a reliable way. With this method a total of ten lifetimes were measured in ^{101}Ag . Due to the complexity of the level scheme, we shall now comment details of this part of the analysis.

The $9/2^+$ ground state of ^{101}Ag is populated via a $\Delta I = 1$ transition of 687 keV from the first excited $11/2^+$ state. Gating on its 174 keV feeder transition permits a DDCM analysis for this state. Figure 2(a) illustrates the intensities of

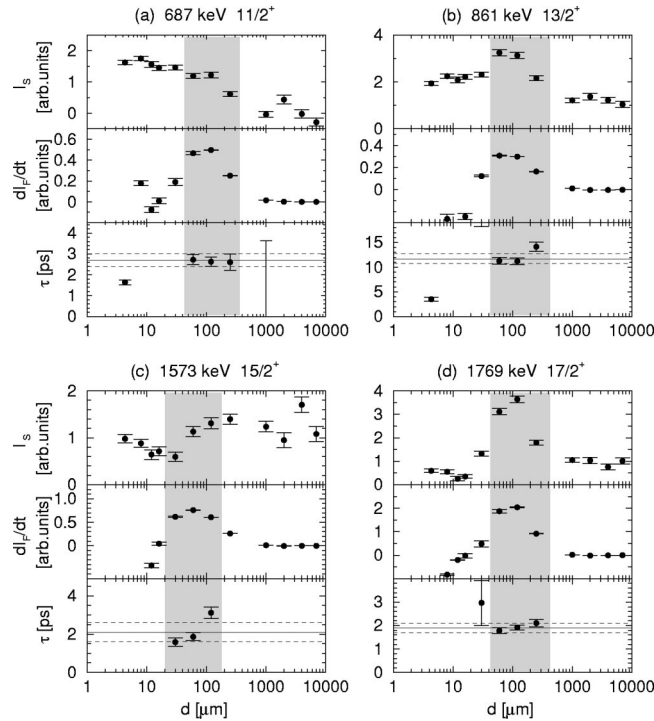


FIG. 2. Differential decay curve (DDCM) analyses of states at positive parity. In each section, the stopped peak intensities, $I_S(d)$, and the derivative of the flight peak intensity, $dI_F(d)/dt$, are plotted as a function of the recoil distance $d = vt$, with a gate set on the flight peak of the populating transition γ_{in} . The hatched areas indicate the adopted lifetime values $\tau = I_S/(dI_F/dt)$. (a) State: 687 keV; decay: 687 keV; gate: 174 keV. (b) State: 861 keV; decay: 174 keV; gate: 908 keV. (c) State: 1573 keV; decay: 712 keV; gate: 196 keV. (d) State: 1769 keV; decay: 908 keV; gate: 248 keV.

the 687 keV stop peak component, $I_S(687)$, and the time derivative of its flight peak component, $dI_F(687)/dt$, gated with the flight peak component of the 174 keV feeder transition. The lifetime $\tau(687) = 2.7(3)$ ps is then obtained as the ratio between them, $\tau = I_S/(dI_F/dt)$. The $13/2^+ \rightarrow 9/2^+$ quadrupole transition of 861 keV is the most intense one in ^{101}Ag , but also one of the most intense transitions in ^{102}Cd populated in the concurrent $\alpha 2p$ evaporation channel [3]. This fact makes the DDCM analysis difficult and therefore, in spite of lower counting statistics, the lifetime of the $13/2^+$ state was deduced by looking at the 174 keV transition and gating on the 908 keV feeder line. With this procedure a lifetime of $\tau = 11.7(10)$ ps for the $13/2^+$ state was obtained [see Fig. 2(b)]. The next state at positive parity is the 1573 keV $15/2^+$ level, which is fed by the 196 keV $M1$ and 444 keV $E2$ transitions and another $\Delta I = 1$ transition of 542 keV, originating from the $17/2$ level at 2115 keV. A lifetime of $\tau = 2.1(5)$ ps is the mean value obtained at the three distances $d = 30$ –120 mm [see Fig. 2(c)]. A possible contamination from another peak in the stop component generated the rather large relative error of about 25% in this lifetime value. The lifetime of the 1769 keV $17/2^+$ state, $\tau = 1.9(2)$ ps, was measured via DDCM by gating on the 248 keV feeder transition and looking at the 908 keV transition [see Fig. 2(d)].

The next state in this cascade, 2017 keV $19/2^+$, is populated by the 939 keV $E2$ transition and by dipole transitions of 604 and 905 keV. The most intense 939 keV feeder line is not accessible for gating, because its flight component overlaps at most angles with the 929 or 948 keV lines, which are

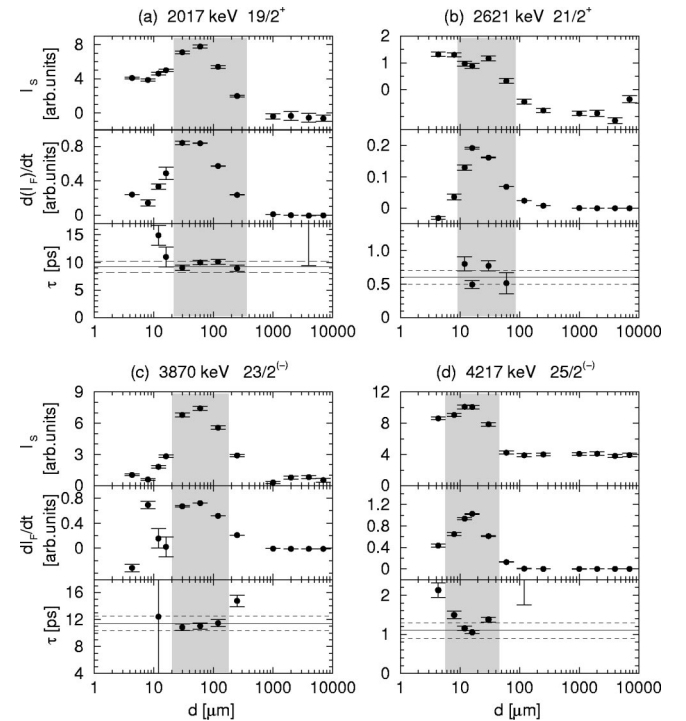


FIG. 3. Same as in Fig. 2, but for other states. (a) State: 2017 keV; decay: 248 keV; gate: 604 keV. (b) State: 2621 keV; decay: 604 keV; gate: 335 keV. (c) State: 3870 keV; decay: 948 keV; gate: 347 keV. (d) State: 4217 keV; decay: 347 keV; gate: 533 keV.

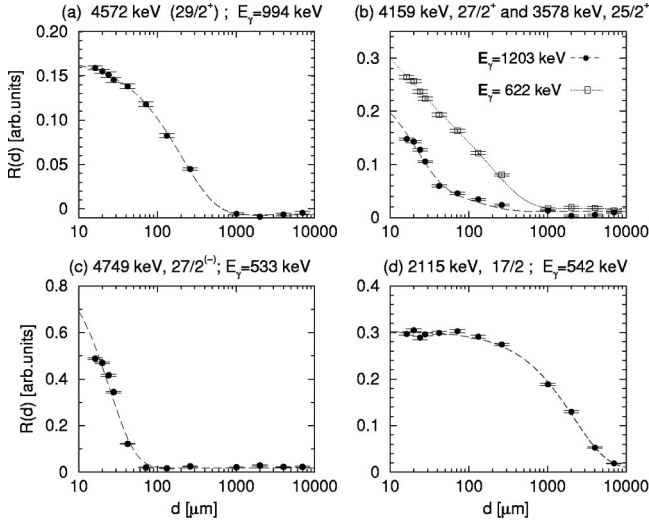


FIG. 4. Decay curves of several transitions which were analyzed using the conventional RDDS method, by gating on subsequent transitions in the cascades. (a) State: 4572 keV; decay: 994 keV; gate: 248 keV. (b) State: 4159 keV; decay: 1203 keV; gate: 248 keV. State: 3578 keV; decay: 622 keV, gate: 248 keV. (c) State: 4749 keV; decay: 533 keV; gate: 347 keV. (d) State: 2115 keV; decay: 542 keV; gate: 712 keV.

in coincidence with the 248 and 444 keV transitions. For this reason a gate on the flight peak of the 604 keV feeder transition was used and the 248 keV decay transition was considered in the analysis [see Fig. 3(a)]. The 335 and 604 transitions in the $\Delta I=1$ band were used as gate and decay line, respectively, in the measurement of the 2621 keV $21/2^+$ state. Its lifetime turned out to be the smallest accessible one in this cascade, $\tau=0.6$ ps [see Fig. 3(b)]. For this state, good agreement was found among the τ values derived at $\theta = 35^\circ$, 59° , and 121° , while at 145° the flight component of the 604 keV transition overlaps with the 622 keV transition. Finally, the lifetime of the highest state at positive parity, 2956 keV $23/2^+$, accessible to DDCM, was measured by gating on the 1203 keV feeder and analyzing the 335 keV transition.

In the supposed negative parity $\Delta I=1$ sequence, lifetimes of 11.4(11) and 1.1(2) ps were deduced for the two lowest states at 3870 and 4217 keV of spins $23/2^{(-)}$ and $25/2^{(-)}$, respectively [Figs. 3(c) and 3(d)]. In order to obtain a better consistency of the results in the $23/2^{(-)}$ state, the spectra at forward angles 35° and 59° were excluded because of a contamination of the flight peak of the 929 keV transition in the 948 keV line.

B. The Conventional RDDS method

Due to their low intensities in the spectra gated from above, conventional RDDS analyses, instead of DDCM, were performed for the highest states in the positive parity band as well as for the $27/2^{(-)}$ state. In this way, three lifetimes and two upper lifetime limits were obtained. Figures 4(a) and 4(b) shows the decay curves $R(d)$ of the yrast states with $I=(29/2^+)$, $27/2^+$, and $25/2^+$. The decay curve of the $29/2^+$ state was fitted through the 994 keV transition, with

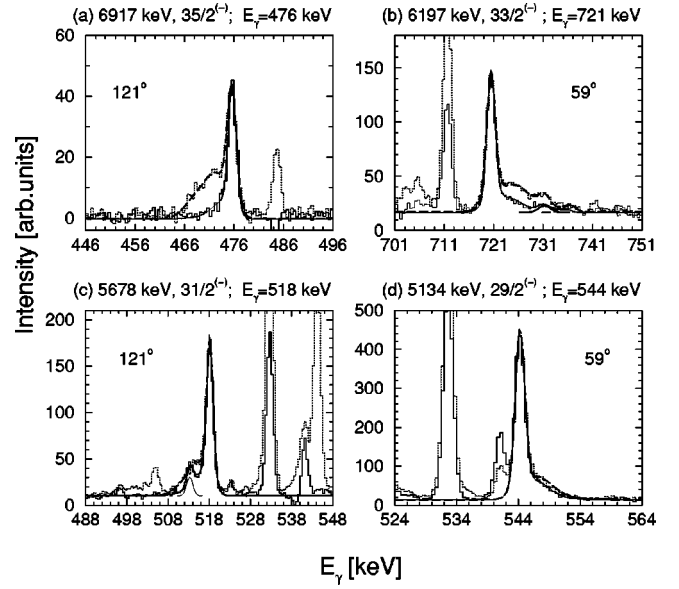


FIG. 5. NGTB analyses of higher lying states (for details see text). (a) State: 6917 keV; γ_{in} : 476 keV; gates: 721, 347 keV. (b) State: 6198 keV; γ_{in} : 721 keV; gates: 518, 347 keV. (c) State: 5678 keV; γ_{in} : 518 keV; gates: 544, 347 keV. (d) State: 5134 keV; γ_{in} : 544 keV; gates: 385, 347 keV.

feeding via the 728 keV transition from the $(31/2^+)$ state and a (continuum) side-feeding component with the adjustable side feeding time τ_{SF} taken into account. [The effective lifetime $\tau_{eff}=1.37(33)$ ps of the $(31/2^+)$ state was measured with the DSA method as will be explained in the next section.]

Among all positive parity levels, the 4572 keV $(29/2^+)$ state appears to have the longest lifetime, $\tau=14(1)$ ps, which also dominates the decay pattern in the subsequent cascade. The decay curves of the 4159 keV $27/2^+$ and 3578 keV $25/2^+$ levels were fitted by using two discrete feeder transitions and a side-feeding component as free parameters. The relatively long side-feeding time and the low counting statistics of these highly excited states introduce errors comparable to the τ values. For that reason, we only adopted upper lifetime limits for the $27/2^+$ state ($\tau < 2.5$ ps) and for the $25/2^+$ state ($\tau < 2.0$ ps).

Similar decay and feeding scenarios were used when performing RDDS analyses for the decay functions of the 4749 keV $27/2^{(-)}$ and 2115 keV $17/2$ states [see Figs. 4(c) and 4(d)]. The former state was fitted with an effective lifetime of 1.8(1) ps, considering the discrete 385 keV feeder plus side population. The latter state, which decays via a dipole transition of 542 keV, clearly represents the longest lifetime measured in this nucleus, $\tau=199(7)$ ps.

C. The DSA and NGTB analyses

As shown in Fig. 1, the yrast bands of stretched transitions are known up to spins $(31/2^+)$ and $(41/2^-)$, respectively. The recoil distance analysis permitted measurements of lifetimes only up to the states of spins $(29/2^+)$ and $27/2^{(-)}$, while the lifetimes of the higher excited states were obtained by using the Doppler shift attenuation (DSA) tech-

TABLE I. Lifetimes of excited states in ^{101}Ag .

State		Lifetime (ps)				
E_x (keV)	I^π	DDCM	RDDS	DSA/NGTB	Adopted	Theory
Positive parity						
98	$7/2^+$					425
687	$11/2^+$	2.7(3)			2.7(3)	2.0
861	$13/2^+$	11.7(10)			11.7(10)	3.4
1573	$15/2^+$	2.1(5)			2.1(5)	0.4
1769	$17/2^+$	1.9(2)			1.9(2)	1.9
2017	$19/2^+$	9(1)			9(1)	5.0
2621	$21/2^+$	0.6(1)			0.6(1)	0.4
2922	$21/2_2^+$					1700 ^a 2.8 ^b
2956	$23/2^+$	1.8(3)			1.8(3)	0.9
3578	$25/2^+$		<2.0		<2.0	0.4
4159	$27/2^+$		<2.5		<2.5	0.3
4572	$(29/2^+)$		14(1)		14(1)	
5300	$(31/2^+)$			≤ 1.7	≤ 1.7	
Negative parity						
750	$3/2^{(-)}$					10.2
797	$5/2^{(-)}$					30.5
3870	$23/2^{(-)}$	11.4(11)			11.4(11)	8.4
4217	$25/2^{(-)}$	1.1(2)			1.1(2)	1.2
4749	$27/2^{(-)}$		1.1(1)		1.1(1)	1.1
5134	$29/2^{(-)}$			0.83(8)	0.83(8)	0.81
5678	$31/2^{(-)}$			0.41(5)	0.41(5)	0.45
6197	$33/2^{(-)}$			0.30(4)	0.30(4)	0.34
6917	$35/2^{(-)}$			0.18(5)	0.18(5)	0.13
7393	$37/2^{(-)}$			≤ 1.3	≤ 1.3	0.39
No parity assigned						
2115	$17/2$		199(7)		199(7)	$\pi = +$ 120 $\pi = -$
3210	$21/2$	1.2(1)			1.2(1)	1.0 2.9
3801	$23/2$					0.5 0.9
4315	$25/2$					0.5 0.4

^aIf wave function predominantly $\pi^3(g_{9/2})$.

^bIf wave function predominantly $\pi(g_{9/2})$.

nique. Again, the lifetimes given in Table I are the average values deduced at the different angles of observation, $\theta = 35^\circ$, 59° , 121° , and 145° . As in the case of RDDS, the DSA method requires good knowledge of the feeding pattern and, of course, is even more dependent on the side-feeding times and intensities. We used the Monte Carlo program LINESHAPE [20], which employs the shell-corrected stopping power function by Northcliffe and Schilling [21] and takes into account the straggling and kinematical spread due to particle evaporation and finite target thickness.

Upper lifetime limits were determined for the highest states in each cascade by means of the conventional DSA method, i.e., by gating on a strong transitions below. Concerning the 5300 keV ($31/2^+$) state, the line shapes of the 728 keV transition at $\theta = 59^\circ$ and 72° , gated by the succeeding 622 keV transition, were fitted via DSA by considering one free parameter, namely the effective lifetime τ_{eff} of the state. In this form, for the 5300 keV ($31/2^+$) state, we ob-

tained $\tau_{eff} = 1.37(33)$ ps, which gave the lifetime limit $\tau \leq 1.7$ ps of this state. [This effective lifetime had been used as input parameter in the RDDS analysis of the cascade ($29/2^+$)– $27/2^+$ – $25/2^+$, as discussed before.] At negative parity the situation concerning the 7393 keV $37/2^{(-)}$ state is very similar. The DSA analysis was carried out for the Doppler profiles of the 476 keV transition at $\theta = 145^\circ$ and 121° , from which we obtained the effective lifetime $\tau_{eff} = 1.2(1)$ ps and the lifetime limit $\tau \leq 1.3$ ps of this state. This effective lifetime was then introduced into the analysis of the subsequent cascade $35/2^{(-)}$ – $33/2^{(-)}$ – $31/2^{(-)}$ – $29/2^{(-)}$.

Brandolini and Ribas have recently developed a “narrow gate on transition below” (NGTB) Doppler shift technique [17], which, like in the case of the DDCM analysis, circumvents the side-feeding problem when introducing appropriate gating conditions. We have adopted this method in the analysis of four states in ^{101}Ag . Examples for line shape fits using

TABLE II. Experimental and calculated transition strengths in ^{101}Ag . The experimental values of b and δ are from [11].

State		Transition				Transition strength [W.u.]				
E_x (keV)	I_i^π	I_f^π	E_γ (keV)	b (%)	$\tan^{-1}\delta$ (deg)	$B(E2)_{Exp}$	$B(E2)_{The}$	$B(M1)_{Exp}(10^{-3})$	$B(M1)_{The}(10^{-3})$	$B(E1)$
Positive parity										
98	$7/2^+$	$9/2^+$	98	100			14		52	
687	$11/2^+$	$9/2^+$	687	100	-20(35)	<36	28	32(15)	36	
861	$13/2^+$	$9/2^+$	861	91(2)		4.8(5)	16			
		$11/2^+$	174	9(2)	-2(2)	≤ 5.2	20	46(11)	180	
1573	$15/2^+$	$13/2^+$	712	84(3)	-11(3)	2.3(13)	25	34(8)	152	
		$11/2^+$	886	16(3)		4.1(17)	20			
1769	$17/2^+$	$13/2^+$	908	87(6)		22(4)	22			
		$15/2^+$	196	13(6)	-4(2)	≤ 71	25	387(136)	268	
2017	$19/2^+$	$15/2^+$	444	8(3)		15(7)	27			
		$17/2^+$	248	92(3)	0(1)	≤ 0.02	22	199(15)	378	
2621	$21/2^+$	$19/2^+$	604	74(3)	-10(15)	≤ 54	20	173(34)	321	
		$17/2^+$	852	26(3)		28(8)	23			
2922	$21/2_2^+$	$19/2_1^+$	905	72(13)			0.004 ^b		0.02 ^b	
		$17/2_1^+$	1153	28(13)			0.004 ^b			
		$19/2_1^+$	905	72(13)			0.04 ^c		10 ^c	
		$17/2_1^+$	1153	28(13)			1.2 ^c			
2956	$23/2^+$	$21/2^+$	335	31(6)	-1(3)	<2.6	15	146(37)	469	
		$19/2^+$	940	69(6)		15(4)	24			
3578	$25/2^+$	$23/2^+$	622	67(6)	-5(4)	>0	12	>40	267	
		$21/2^+$	957	33(6)		>5	14			
4159	$27/2^+$	$25/2^+$	581	18(6)			8.6	>8	439	
		$23/2^+$	1203	82(6)			14			
4572	$(29/2^+)$	$27/2^+$	413	18(13)				5.7(41)		
		$25/2^+$	994	82(13)		1.7(3)				
5300	$(31/2^+)$	$29/2^+$	728	28(7)	-1(3)			≥ 10		
		$27/2^+$	1141	72(7)		≥ 6				
Negative parity										
750	$3/2_1^-$	$1/2_1^-$	476	n.o.			28		22	
797	$5/2_1^-$	$3/2_1^-$	47	n.o.			0.25		3.5	
		$1/2_1^-$	523	n.o.			25			
3870	$23/2^{(-)}$	$23/2^+$	913	30(9)					$1.5(5)10^{-5}$	
		$21/2^+$	948	35(9)					$1.6(4)10^{-5}$	
		$21/2^{(-)}$	74	22(9)			15	688(289)	995	
4217	$25/2^{(-)}$	$23/2^{(-)}$	347	86(2)	1(1)	<4.3	15	595(109)	646	
		$23/2$	416 ^a	14(2)	-2(5)	≤ 2.2		56(12)	$79(18)10^{-5}$	
4749	$27/2^{(-)}$	$25/2^{(-)}$	533	76(4)	0(2)	≤ 0.5	16	145(15)	145	
		$23/2^{(-)}$	880	17(4)		8.5(28)	13			
		$25/2^{(-)}$	435	7(4)	4(4)	≤ 1.7		24(14)		
5134	$29/2^{(-)}$	$27/2^{(-)}$	385	76(2)	3(1)	8.7(58)	20	509(51)	487	
		$25/2^{(-)}$	918	24(2)		12.9(23)	16			
5678	$31/2^{(-)}$	$29/2^{(-)}$	544	90(3)	0(1)	≤ 1.2	18	434(54)	325	
		$27/2^{(-)}$	929	10(3)		10.2(43)	22			
6197	$33/2^{(-)}$	$31/2^{(-)}$	518	82(5)	3(4)	≤ 18	18	624(92)	447	
		$29/2^{(-)}$	1063	18(5)		12.9(53)	22			
6917	$35/2^{(-)}$	$33/2^{(-)}$	721	69(8)	2(5)	≤ 2	15	325(98)	451	
		$31/2^{(-)}$	1239	31(8)		17(9)	20			
7393	$37/2^{(-)}$	$35/2^{(-)}$	476	65(7)	4(4)	≥ 0	11	≥ 146	407	
		$33/2^{(-)}$	1197	35(7)		≥ 3.2	14			

TABLE II. (*Continued*).

State		Transition				Transition strength [W.u.]				
E_x (keV)	I_i^π	I_f^π	E_γ (keV)	b (%)	$\tan^{-1} \delta$ (deg)	$B(E2)_{Exp}$	$B(E2)_{The}$	$B(M1)_{Exp}(10^{-3})$	$B(M1)_{The}(10^{-3})$	$B(E1)$
No parity assigned ($\pi = +$)										
2115	$17/2_2^{(+)}$	$17/2^+$	346	n.o.			0.004		1.8	
		$15/2^+$	542	100				1.0(4)		0.7
		$13/2^+$	1254	n.o.		0.02				
3210	$21/2_3^{(+)}$	$17/2_2^{(+)}$	1095	100		16(2)	13			
		$19/2_1^+$	1193	n.o.			0.003		1.5	
3801	$23/2_2^{(+)}$	$21/2_3^{(+)}$	591	100	$-10(10)$		20		239	
4315	$25/2_2^{(+)}$	$23/2_2^{(+)}$	514	100	$-7(10)$		21		361	
		$21/2_3^{(+)}$	1105	n.o.			16			
No parity assigned ($\pi = -$)										
2115	$17/2^{(-)}$	$15/2^+$	542	100						1.4(5) 10^{-5}
3210	$21/2^{(-)}$	$17/2_2^{(-)}$	1095	100		16(2)	3.1			
3801	$23/2^{(-)}$	$21/2_3^{(-)}$	591	100	$-10(10)$		11		138	
4315	$25/2^{(-)}$	$23/2_2^{(-)}$	514	100	$-7(10)$		25		521	
		$21/2_3^{(-)}$	1105	n.o.			2			

^a $E1$ or $M1/E2$ are possible.

^bIf wave function predominantly $\pi^3(g_{9/2})$.

^cIf wave function predominantly $\pi(g_{9/2})$.

NGTB are displayed in Figs. 5(a)–5(d). The NGTB method can be summarized as follows: one observes the Doppler shifted lineshape of a transition γ_{in} populating the state being studied having the lifetime τ , by gating onto different portions of the Doppler broadened line profile of a transition γ_{out} depopulating the state investigated. Depending on the state lifetime τ and the chosen gate window of γ_{out} , the lineshape and intensity of γ_{in} will change. As an example, let us consider the NGTB analysis of the 6917 keV $35/2^{(-)}$ state, at $\theta = 121^\circ$, which is fed by the 476 keV transition (γ_{in}) and decays via the 721 keV transition (γ_{out}). The two lineshapes of γ_{in} shown in Fig. 5(a) were obtained, by either gating on the 347 keV $25/2^{(-)} \rightarrow 23/2^{(-)}$ transition which only shows a stopped component, or on the stopped component of the Doppler broadened 721 keV line γ_{out} . These two lineshapes of γ_{in} , which are indicated as dashed and full lines in Fig. 5(a), are clearly different and give the lifetime $\tau(35/2^{(-)}) = 0.18(5)$ ps. NGTB line shape analyses were also performed for the subsequent states in this cascade at 6197, 5678, and 5134 keV and the corresponding fits are displayed in Figs. 5(b)–5(d), providing the lifetimes $\tau(33/2^{(-)}) = 0.30(4)$ ps, $\tau(31/2^{(-)}) = 0.41(5)$ ps and $\tau(29/2^{(-)}) = 0.83(8)$ ps, respectively.

D. Summary of experimental transition strengths

Using the γ -ray energies shown in Fig. 1 and their known branching and mixing ratios [11], we determined the reduced transition strengths $B(M1)$, $B(E2)$ and, $B(E1)$ listed in Table II. For the low-energy transitions, electron conversion was taken into account. For all stretched $\Delta I = 1$ transitions, we either used the published mixing ratios or assumed pure dipole character. At both parities, the $E2$ transitions are moderately enhanced [up to 30 Weisskopf units (W.u.)]. The $M1$ strengths at positive parity up to spin 15/2 are very weak

(some 40 m W.u.), but increase to 150–400 m W.u. in the spin range $17/2^+ - 23/2^+$. At negative parity, we find large $M1$ strengths of 200–700 m W.u. in the spin range $23/2^- - 35/2^-$.

As pointed out before, the group of states at 2115, 3210, 3801 and 4315 keV excitation having spins of $I = 17/2 - 25/2$ has not been given definite parity. This group is fed from the negative parity yrast levels (via the 586, 416, and 435 keV γ rays) and finally decays to the 1573 keV $15/2^+$ state (via the 542 keV γ ray). Not knowing the parities of this group of levels, we have listed alternatively the $M1$ and/or $E1$ strengths of the relevant transitions. If we assume positive parity for this group, the feeding transitions (416 and 435 keV) are of $E1$ character and are of normal retardation ($\sim 10^{-5}$ W.u.); the 542 keV depopulating $M1$ transition would be very weak (1 m W.u.). On the other hand, if we assume negative parity for the group, we find $M1$ feeders (416, 435 keV) of normal size and the 542 keV $E1$ transition features the typical retardation of about 10^{-5} W.u. On the basis of the transition strengths, it was not possible to distinguish between these two possibilities.

IV. INTERPRETATION WITHIN THE INTERACTING BOSON-FERMION PLUS BROKEN PAIR MODEL

In this section we apply the interacting boson/interacting boson-fermion model [22–25] (IBM/IBFM) in the analysis of positive and negative parity structures in ^{101}Ag . Models based on the interacting boson approximation have been very successfully employed in the description of a variety of nuclear structure phenomena. In particular, for a description of high-spin states the IBM/IBFM model space has to be extended by including part of the original shell-model fermion space through successive breaking of correlated S and

D pairs (s and d bosons). Here we briefly outline the essential features of the model for even-even [26], and odd-even [27] nuclei. The approach is based on the simplest version of the IBM/IBFM models: the boson space consists of s and d bosons, no distinction is made between proton and neutron bosons. High-spin states are generated not only by the alignment of d bosons, but also by coupling fermion pairs to the boson core. A boson can be destroyed, i.e., a correlated fermion pair can be broken, by the Coriolis interaction, and the resulting noncollective fermion pair recouples to the core. The structure of high-spin states is therefore determined by broken pairs. The model with one and two broken pairs for *even-even* nuclei has been applied to the description of high-spin states in the Hg [26–28], Sr-Zr [29–31], Nd-Sm [32–35], and Cd [4] regions. In Ref. [27] the interacting boson fermion model for *odd-even* nuclei has been extended to include one broken pair and applied to the analysis of high-spin states of Hg isotopes. The model for odd-even nuclei has also been used to calculate the structure of low and high spin states, as well as the electromagnetic properties of ^{139}Sm [32], ^{137}Nd [34], and ^{97}Y [36]. As compared with traditional models based on the cranking scheme, the IBM/IBFM approach has the advantage that all calculations are performed in the laboratory system and provide results directly comparable with experimental data.

The model space for an odd-even nucleus with $2N+1$ valence nucleons reads

$$|(N)\text{bosons} \otimes 1 \text{ fermion}\rangle \oplus |(N-1)\text{bosons} \otimes 1 \text{ broken pair} \otimes 1 \text{ fermion}\rangle.$$

The two fermions in the broken pair can be of the same type as the unpaired fermion, resulting in a space with three identical fermions. If the fermions in the broken pair are different from the unpaired one, the fermion basis contains two protons and one neutron or vice versa. The model Hamiltonian has four terms: the IBM-1 boson Hamiltonian [23], the fermion Hamiltonian, the boson-fermion interactions of IBFM-1 [25], and a pair breaking interaction that mixes states with a different number of fermions:

$$V_{\text{mix}} = -U_0 \left\{ \sum_{j_1 j_2} u_{j_1} u_{j_2} (u_{j_1} v_{j_2} + u_{j_2} v_{j_1}) \times \langle j_1 \| Y_2 \| j_2 \rangle^2 \frac{1}{\sqrt{2j_2+1}} ([a_{j_2}^\dagger \times a_{j_2}^\dagger]^{(0)} s) + \text{H.c.} \right\} - U_2 \left\{ \sum_{j_1 j_2} (u_{j_1} v_{j_2} + u_{j_2} v_{j_1}) \langle j_1 \| Y_2 \| j_2 \rangle \times ([a_{j_1}^\dagger \times a_{j_2}^\dagger]^{(2)} \bar{d}) + \text{H.c.} \right\}. \quad (1)$$

If the three-fermion basis consists of proton and neutron states (the broken-pair nucleons and the odd nucleon are of different type), there will be two boson-fermion interaction terms in the Hamiltonian. Most of the parameters of the model Hamiltonian are taken from analyses of low and high-

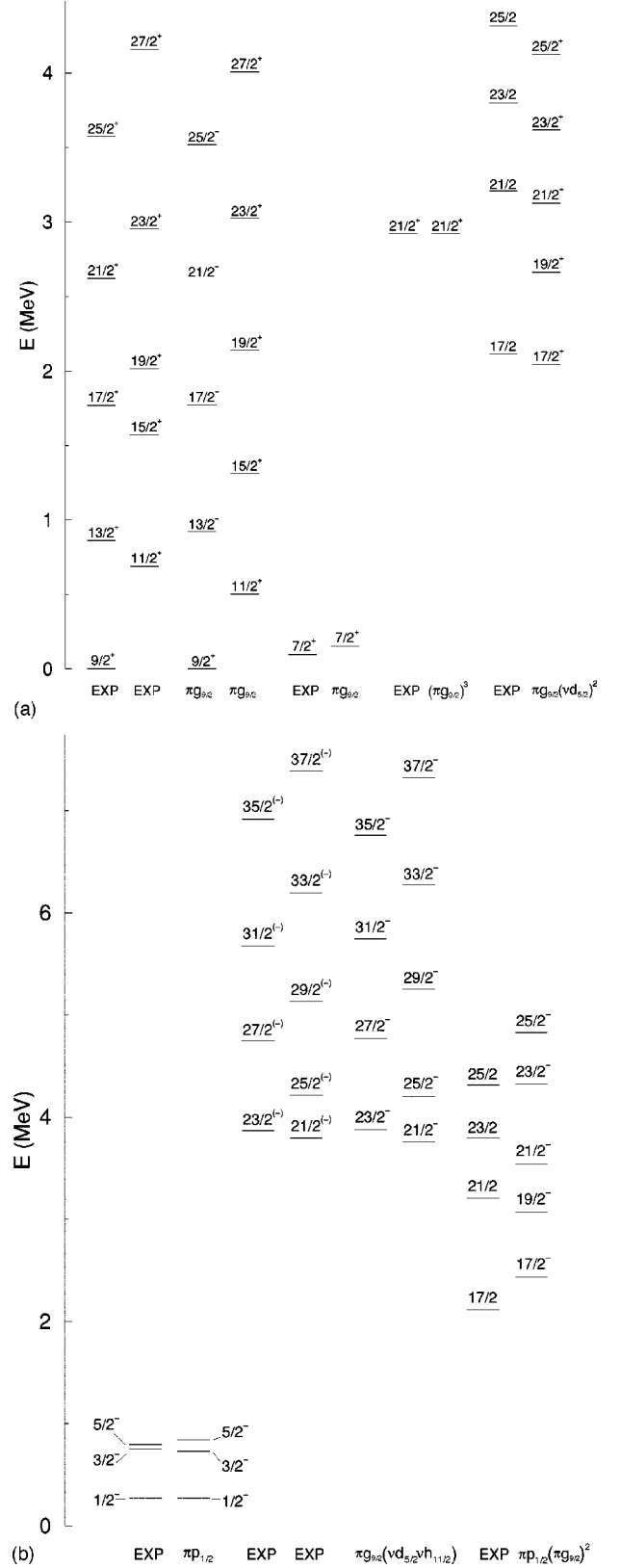


FIG. 6. Experimental level scheme and fit with the interacting boson fermion plus broken pair model. The band heads are labeled by their fermion character. (a) Positive parity. (b) Negative parity.

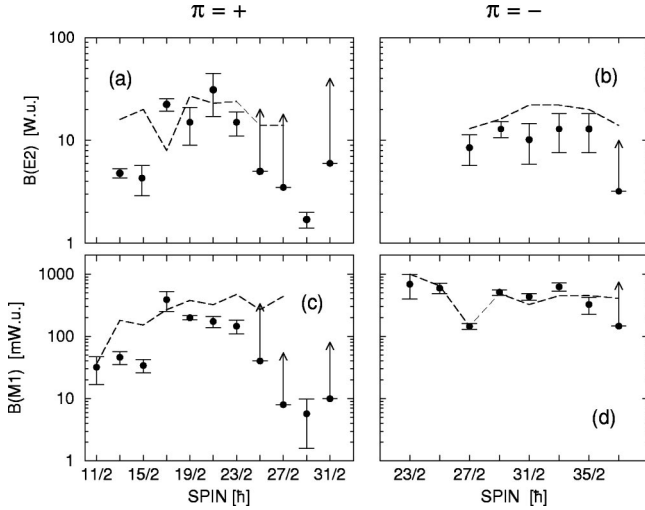


FIG. 7. Comparison between measured (filled circles) reduced E2 (a), (b) and M1 (c), (d) transition strengths and the results of calculations within IBFBP model (dashed lines).

spin states in neighboring even and odd- A nuclei. Only a minimal number of model parameters is adjusted to the high-spin structure of a specific nucleus.

In the present analysis of ^{101}Ag we take as the core nucleus: $^{102}_{48}\text{Cd}$. This nucleus displays a transitional structure between the pure shell-model spectrum of ^{100}Cd and the vibrational spectrum of ^{104}Cd . The structure of low and high-spin states of both parities in ^{104}Cd has recently been described in the framework of the interacting boson model plus one-broken pair [4,5]. The set of parameters for the boson Hamiltonian is (all values in MeV): $\epsilon=0.78$, $C_0=0.3$, $C_2=0.2$, $C_4=0$, $V_2=0$, and $V_0=0$. The number of bosons in the IBM scheme is equal to half the number of ν valence nucleon particles and holes. For ^{102}Cd this is three. Such a small number of bosons, however, does not account for the observed collective properties of both ^{102}Cd and ^{101}Ag . Somewhat arbitrarily, we have chosen the number of bosons $N=5$. A larger value of the boson number would result in prohibitively large dimensions of the model bases for ^{101}Ag . The calculated excitation spectrum of ^{102}Cd corresponds to the SU(5) dynamical symmetry limit of the IBM, and nicely reproduces the low-lying states observed in the experimental spectrum.

The fermion space of proton single-quasiparticle states contains the orbitals: $f_{5/2}$ ($E=3.621$ MeV, $v^2=0.99$), $p_{3/2}$ ($E=2.997$ MeV, $v^2=0.98$), $p_{1/2}$ ($E=1.946$ MeV, $v^2=0.96$), $g_{9/2}$ ($E=1.696$ MeV, $v^2=0.72$), and $d_{5/2}$ ($E=7.696$ MeV, $v^2=0.003$). The single-quasiparticle energies and occupation probabilities are obtained by a simple BCS calculation using Kisslinger-Sorensen [37] single-particle energies. The calculated quasiparticle energy of the $g_{9/2}$ orbital, however, was increased by 800 keV in order to reproduce the relative positions of the observed bands. This additional shift brings the $g_{9/2}$ orbital much closer to the $p_{1/2}$ level, in accordance with experimental data. The parameters of the proton fermion-boson interactions are $\Gamma_0=0.55$ MeV and $\chi=-0.9$ for the dynamical interaction, $\Lambda_0=1.8$ MeV for the exchange interaction, and $A_0=0.1$ MeV for the mono-

pole interaction. The values of Γ_0 and Λ_0 are identical to those used in the calculation of the odd-odd neighbor ^{102}Rh [38], and only the value of A_0 has been slightly increased by 0.03 MeV. The value of the parameter χ in the boson quadrupole operator is taken from the calculations of ^{104}Cd [5] and ^{102}Rh [38]. $\chi=-0.9$ in the E2 operator, together with the vibrational charge $e^{vib}=1.5$, reproduces the $B(E2)$ values for the transitions between the low-lying states of the core nucleus ^{102}Cd , and the calculated quadrupole moment $Q(2^+_1)=-0.172$ eb is in agreement with the systematics of this mass region. The strength parameter of the proton pair-breaking interaction is $U_2=0.2$ MeV, and the residual interaction between unpaired protons is a surface δ force with the strength $v_0=-0.15$ MeV.

The neutron quasiparticle energies and occupation probabilities have been calculated with the Reehal-Sorensen parametrization of the single-neutron energies [39]. The present calculation includes the neutron orbitals $d_{5/2}$ ($E=1.013$ MeV, $v^2=0.44$), $g_{7/2}$ ($E=2.02$ MeV, $v^2=0.11$), and $h_{11/2}$ ($E=2.549$ MeV, $v^2=0.03$). The parameters of the neutron fermion-boson interactions are the strength of the dynamical interaction is $\Gamma_0=0.5$ MeV for positive parity states, and $\Gamma_0=0.2$ MeV in the calculation of states of negative parity, $\chi=-0.9$ in the boson quadrupole operator, $\Lambda_0=0.2$ MeV for the exchange interaction, the strength parameter of the monopole interaction is $A_0=-0.04$ MeV for $\pi=+1$ states, and $A_0=-0.03$ MeV for $\pi=-1$ states. The values of the neutron fermion-boson interaction parameters are very similar to those used in the calculation of high-spin states based on neutron two-quasiparticle states in ^{104}Cd . The strength parameter of the neutron pair-breaking interaction is $U_2=0.15$ MeV, and the strength of the δ interaction between unpaired neutrons is $v_0=-0.03$ MeV.

From the calculation of the odd-even ^{101}Rh and the odd-odd ^{102}Rh [38] we take the quadrupole-quadrupole residual interaction between the unpaired protons and unpaired neutrons, with the strength parameter $v^{\pi\nu}=-0.5$ MeV.

In Fig. 6(a) we compare the experimental spectrum of positive-parity states with results of the present calculation. Only those calculated states are shown which have an experimental counterpart. For the low-spin part, the excitation spectrum displays a weakly coupled structure based on the proton $g_{9/2}$ orbital. The lowest structure of favored states is very well reproduced by the calculated band based on the $9/2^+_1$ state. The band of unfavored states displays an anomaly around 2 MeV (between the states $15/2^+_1$ and $19/2^+_1$) which could not be obtained in the theoretical spectrum. In the core nucleus ^{102}Cd , at the same excitation energy, a decrease in the energy gap between the yrast states 4^+ and 6^+ is observed, which is not reproduced by our choice of a pure SU(5) vibrational core. The calculation reproduces the position of the low-lying $7/2^+_1$ state, and that of the lowest three-proton state $(\pi g_{9/2})^3 21/2^+$. This state, which is the bandhead of the lowest $(\pi g_{9/2})^3$ band, has a possible experimental counterpart at 2922 keV, although the experimental level could also belong to the yrare $\pi g_{9/2}$ structure. The half-life of this level is not known. If it was an isomer, then of course it could be assigned to the $(\pi g_{9/2})^3$ band.

The parity of the sequence of experimental states (17/2,21/2,23/2,25/2) shown on the right-hand side of Fig. 1, has not been determined yet. The measured mean-life $\tau(17/2)=199(7)$ ps excludes the possibility that this state belongs to one of the side bands based on the single-proton $g_{9/2}$ configuration. We have compared the experimental structure with the calculated one proton–two neutron band $\pi g_{9/2}(\nu d_{5/2})^2$. The excitation energies of the experimental sequence are in good agreement with the calculated positive parity band based on the band-head $17/2^+$. This $\Delta I=1$ band, however, contains also the level with spin $19/2^+$, which has not been observed experimentally.

The calculated and experimental states of negative parity are compared in Fig. 6(b). Again, only those theoretical levels are shown which have a possible experimental counterpart. The calculation reproduces the triplet of low-lying states based on the proton $p_{1/2}$ orbital [18]. Above 4 MeV excitation energy, two $\Delta I=2$ sequences of probably negative parity states are observed, based on the band heads $21/2^{(-)}$ and $23/2^{(-)}$, respectively. These two sequences are very well reproduced by the two lowest $\Delta I=2$ bands based on the one proton–two neutron configuration $\pi g_{9/2}(\nu d_{5/2}, \nu h_{11/2})$. We notice an almost perfect correspondence between the calculated and experimental levels, up to the highest observed angular momenta.

In addition to the comparison shown on the right-hand side of Fig. 6(a), we have also investigated the possibility that the experimental sequence 17/2, 21/2, 23/2, and 25/2 is of negative parity. In Fig. 6(b) the experimental levels are compared with the lowest three-proton band $\pi p_{1/2}(\pi g_{9/2})^2$. In the calculation of this structure, in particular, the strength of the dynamical proton fermion-boson interaction has been increased to $\Gamma_0=0.9$ MeV. A reasonable agreement is observed, and therefore we cannot exclude the assignment of either positive or negative parity to the experimental sequence.

In Table I we compare the experimental and calculated lifetimes. The experimental and calculated $B(E2)$ and $B(M1)$ values for transitions in ^{101}Ag are compared in Table II and shown in Fig. 7. For the effective charges and gyromagnetic ratios the following values have been used: $e^{vib}=1.5$, $e^\pi=1.5$, $e^\nu=0.5$, $g_R=0.4$, $g_l^\pi=1.0$, g_s^π

$=0.4$ $g_s^{\pi,free}=2.234$, the gyromagnetic factor which multiplies the tensor operator $(Y_2\vec{S})_1: g_T^\pi=1/30\langle r^2\rangle g_s^{\pi,free}=3.489$, $g_l^\nu=0.0$, $g_s^\nu=0.4$ $g_s^{\nu,free}=-1.530$.

The calculation reproduces the measured $B(E2)$ and $B(M1)$ values for transitions among states based both on single-proton and three-fermion configurations. In particular, we notice the excellent agreement of the calculated and experimental mean lives. For the sequence of unknown parity states based on 17/2 at 2115 keV, the theoretical $B(E2)$ and $B(M1)$ values do not discriminate between the two possible parity assignments. In both cases a strong transition to the unobserved 19/2 state was predicted.

V. CONCLUSIONS

We have presented measurements of a large number of lifetimes of high-spin states in ^{101}Ag by means of various $\gamma\gamma$ -coincidence Doppler shift techniques and have deduced a comprehensive set of $M1$, $E2$, and $E1$ transition strengths from them. By employing the DDCM and NGTB techniques, we have circumvented uncertainties due to continuum side feeding, for most part of the analysis.

Having three proton holes and four neutron particles relative to the double shell closure ^{100}Sn , the number of valence nucleons is already rather large and may justify the use of the interacting boson fermion model involving either an additional broken neutron or proton pair. Many details of the decay scheme are well reproduced with this approach. On the other hand, the limited number of valence nucleons makes this nucleus still accessible to multiparticle shell model calculations, similar to the ones presented in our recent ^{102}Cd and $^{104,105}\text{In}$ studies [3,6], which showed a very high sensitivity to the single particle energies and two-body matrix elements used. It appears that such shell model calculations may shed some light on the microscopic basis of the interacting boson Fermion model in this mass region.

ACKNOWLEDGMENTS

The authors are most grateful to the crew operating the XTU tandem at Legnaro and the hospitality, which LNL granted to them. This work was funded by Deutsches Bundesministerium für Bildung und Forschung and DAAD, Bonn.

-
- [1] D. Alber *et al.*, Z. Phys. A **344**, 1 (1992); R. Schubart *et al.*, Phys. Scr. **T56**, 311 (1995).
 [2] S. Rastikerdar *et al.*, J. Phys. G **22**, 1037 (1996); J. Persson *et al.*, Nucl. Phys. **A627**, 101 (1997).
 [3] K.P. Lieb *et al.*, Phys. Rev. C **63**, 054304 (2001).
 [4] G. de Angelis *et al.*, Phys. Rev. C **60**, 014313 (1999).
 [5] G. A. Müller *et al.*, Phys. Rev. C **64**, 014305 (2001); G. A. Müller, diploma thesis, Göttingen, 2000.
 [6] D. Kast *et al.*, Eur. Phys. J. A **3**, 115 (1998); O. Yordanov *et al.* (unpublished); O. Yordanov, doctoral thesis, Göttingen, 2000.
 [7] C. Broude *et al.*, Z. Phys. A **336**, 133 (1990); C.M. Baglin, Nucl. Data Sheets **80**, 1 (1997).
 [8] A. Jungclaus *et al.*, Nucl. Phys. **A637**, 346 (1998); Phys. Rev. C **60**, 014309 (1999).
 [9] A. Jungclaus *et al.*, Eur. Phys. J. A **6**, 29 (1999).
 [10] D. Alber *et al.*, Z. Phys. A **332**, 129 (1989); L.K. Peker, Nucl. Data Sheets **68**, 165 (1993).
 [11] B. Crowell *et al.*, Phys. Rev. C **45**, 1564 (1992).
 [12] K. P. Lieb, in *Experimental Techniques in Nuclear Physics*, edited by D. N. Poenaru and W. Greiner, (de Gruyter, Berlin, New York, 1997), p. 425.
 [13] A. Dewald *et al.*, Nucl. Phys. **A545**, 822 (1992).
 [14] C. Rossi Alvarez, Nucl. Phys. News Europe **3**, 10 (1993).
 [15] G. Böhm *et al.*, Nucl. Instrum. Methods Phys. Res. A **329**, 248 (1993).

- [16] A. Dewald, S. Harrisopulos, and P. von Brentano, *Z. Phys. A* **334**, 163 (1989).
- [17] F. Brandolini and R. Ribas, *Nucl. Instrum. Methods Phys. Res. A* **417**, 150 (1998).
- [18] A.W.B. Kalshofen *et al.*, *Nucl. Phys.* **A346**, 147 (1980).
- [19] J. Tréherne *et al.*, *Nucl. Phys.* **A342**, 357 (1980).
- [20] J.C. Wells *et al.*, LINESHAPE: A Computer Program for Doppler Broadened Lineshape Analysis, ORNL Physics Division Progress Report 30, 1991, No. ORNL-66B9.
- [21] L.C. Northcliffe and R.F. Schilling, *Nucl. Data, Sect. A* **7**, 233 (1970).
- [22] A. Arima and F. Iachello, *Phys. Rev. Lett.* **35**, 1069 (1975).
- [23] F. Iachello and A. Arima, *The Interacting Boson Model* (Cambridge University Press, Cambridge, 1987).
- [24] F. Iachello and O. Scholten, *Phys. Rev. Lett.* **43**, 679 (1979).
- [25] F. Iachello and P. Van Isacker, *The Interacting Boson-Fermion Model* (Cambridge University Press, Cambridge, 1991).
- [26] F. Iachello and D. Vretenar, *Phys. Rev. C* **43**, 945 (1991).
- [27] D. Vretenar, G. Bonsignori, and M. Savoia, *Z. Phys. A* **351**, 289 (1995).
- [28] D. Vretenar, G. Bonsignori, and M. Savoia, *Phys. Rev. C* **47**, 2019 (1993).
- [29] P. Chowdhury *et al.*, *Phys. Rev. Lett.* **67**, 2950 (1991).
- [30] C.J. Lister, P. Chowdhury, and D. Vretenar, *Nucl. Phys.* **A557**, 361c (1993).
- [31] A.A. Chisthi *et al.*, *Phys. Rev. C* **48**, 2607 (1993).
- [32] C. Rossi Alvarez *et al.*, *Phys. Rev. C* **54**, 57 (1996).
- [33] G. de Angelis *et al.*, *Phys. Rev. C* **49**, 2990 (1994).
- [34] C.M. Petrache *et al.*, *Nucl. Phys.* **A617**, 228 (1997).
- [35] D. Vretenar *et al.*, *Phys. Rev. C* **57**, 675 (1998).
- [36] G. Lhersonneau *et al.*, *Phys. Rev. C* **57**, 681 (1998).
- [37] L.S. Kisslinger and R.A. Sorensen, *Rev. Mod. Phys.* **35**, 853 (1963).
- [38] J. Gizon *et al.*, *Nucl. Phys.* **A658**, 97 (1999).
- [39] B.S. Reehal and R.A. Sorensen, *Phys. Rev. C* **2**, 819 (1970).